energies

MDPI

Article

A New Model for Predicting Permeability of Chang 7 Tight Sandstone Based on Fractal Characteristics from High-Pressure Mercury Injection

Yuxuan Yang [1,2], Zhigang Wen [1,2,*], Weichao Tian [1,2,*], Yunpeng Fan [1,2] and Heting Gao [1,2]

[1] Hubei Key Laboratory of Petroleum Geochemistry and Environment, Yangtze University, Wuhan 430100, China; 2021710450@yangtzeu.edu.cn (Y.Y.); 201404152@yangtzeu.edu.cn (Y.F.); 2021710491@yangtzeu.edu.cn (H.G.)

[2] College of Resources and Environment, Yangtze University, Wuhan 430100, China

* Correspondence: wzg728@sina.com (Z.W.); 520044@yangtzeu.edu.cn (W.T.); Tel.: +86-139-0861-8531 (Z.W.); +86-156-1049-3492 (W.T.)

Abstract: Accurately predicting permeability is important to elucidate the fluid mobility and development potential of tight reservoirs. However, for tight sandstones with the same porosity, permeability can change by nearly three orders of magnitude, which greatly increases the difficulty of permeability prediction. In this paper, we performed casting thin section, scanning electron microscopy and high-pressure mercury injection experiments to analyze the influence of pore structure parameters and fractal dimensions on the permeability of Chang 7 tight sandstones. Furthermore, the key parameters affecting the permeability were optimized, and a new permeability prediction model was established. The results show that the pore throat structure of Chang 7 tight sandstone exhibits three-stage fractal characteristics. Thus, the pore throat structure was divided into large pore throat, medium pore throat and small pore throat. The large pore throat reflects the microfracture system, whose fractal dimension was distributed above 2.99, indicating that the heterogeneity of the large pore throat was the strongest. The medium pore throat is dominated by the conventional pore throat system, and its fractal dimension ranged from 2.378 to 2.997. Small pore throats are mainly composed of the tree-shaped pore throat system, and its fractal dimension varied from 2.652 to 2.870. The medium pore throat volume and its fractal dimension were key factors affecting the permeability of Chang 7 tight sandstones. A new permeability prediction model was established based on the medium pore throat volume and its fractal dimension. Compared to other models, the prediction results of the new model are the best according to the analysis of root mean square value, average absolute percentage error and correlation coefficient. These results indicate that the permeability of tight sandstones can be accurately predicted using mesopore throat volume and fractal dimension.

Keywords: Ordos Basin; Chang 7 tight sandstone; high-pressure mercury injection; fractal dimension; permeability prediction

Citation: Yang, Y.; Wen, Z.; Tian, W.; Fan, Y.; Gao, H. A New Model for Predicting Permeability of Chang 7 Tight Sandstone Based on Fractal Characteristics from High-Pressure Mercury Injection. *Energies* **2024**, *17*, 821. https://doi.org/10.3390/en17040821

Academic Editors: Reza Rezaee and Pål Østebø Andersen

Received: 20 December 2023
Revised: 2 February 2024
Accepted: 5 February 2024
Published: 8 February 2024

1. Introduction

With the continuous reduction in conventional oil and gas reserves, unconventional resources have gradually become an important field of exploration and development [1–3]. Tight oil development has been successful in the United States. As of 2018, the production of tight oil reservoirs has reached nearly 60% of the total oil production in the United States [4]. In China, the total amount of tight oil resources is also quite rich and mainly distributed in the Ordos, Junggar and Songliao basins. However, due to the late start, the tight oil reservoirs in China face great challenges in terms of commercial development [5–7].

Tight reservoirs usually experience extreme compaction and cementation, resulting in lower porosity (mainly <10%) and matrix permeability (mainly <1 mD) [8]. For tight reservoirs, the throats are fine (mainly <1 μm) and mostly in the shape of flakes, bent flakes

and tube bundles, resulting in poor pore connectivity [9–11]. As a result, fluid flow in tight reservoirs is irregular and nonlinear. Additionally, for tight sandstones with the same porosity and different pore structures, the permeability can span nearly two to three orders of magnitude [12,13], which greatly increases the difficulty of quantitatively evaluating permeability. However, quantitative evaluation of permeability is crucial to understanding fluid mobility and evaluating reservoir quality [14].

Permeability is a macroscopic description of rock pore structure and directly affects oil and gas productivity. Permeability can be measured directly in a laboratory based on steady-state methods and unsteady-state methods [15]. For tight reservoirs, these methods are time consuming or expensive. Therefore, statistical methods are often used to evaluate permeability based on the relationship between permeability and porosity [16–18]. Hui et al. (2023) established the relationship between permeability and porosity of shale [17]. However, the relationship between permeability and porosity is usually poor for tight reservoirs with complex pore structures. Pore structure is the key parameter controlling the permeability of tight reservoirs [19]. Thus, the permeability prediction model can be established based on pore structure parameters. At present, a variety of testing methods have been widely used to study reservoir pore structure, including low-temperature nitrogen adsorption, high-pressure mercury injection (HPMI), nuclear magnetic resonance (NMR), scanning electron microscope (SEM) and CT [20–23].

Early permeability prediction models can be divided into three categories: (1) based on HPMI data, (2) based on NMR data and (3) based on fractal theory (Table 1). Purcell (1949) first established a permeability prediction equation using HPMI data [24]. Subsequently, Swanson (1981) utilized the Swanson parameter (the maximum value of S_{Hg}/P_c) to develop a permeability prediction model [25]. Based on Swanson's work, Pittman (1992) established the relationship between permeability, porosity and r_{apex} (the pore throat radius corresponding to the maximum value of S_{Hg}/P_c) [26]. Based on the derivation of the Thomeer model (1983), Guo et al. [27] constructed a parameter (i.e., S_{Hg}/P_c^2) to describe the pore structure of rock and established a permeability prediction model. Winland introduced a relationship between permeability, porosity and pore throat radius at a mercury injection saturation of 35% [28]. Similarly, Rezaee et al. [8] derived the R_{10} model for tight gas sandstone.

Table 1. Common permeability prediction models. K is the permeability and φ is the porosity.

Model Name	Expression
Purcell model	$K = \frac{F(\sigma\cos\theta)^2\varphi}{2\times10^4}\int_0^{100}\frac{dS_{HG}}{P_c^2}$
Winland model	$\lg R_{35} = 0.732 + 0.588\lg K - 0.864\lg\varphi$
Swanson model	$K = 399\left(\frac{S_{Hg}}{P_c}\right)_{apex}^{1.691}$
Thomeer model	$K = 3.806F^{-1.3334}\left(\frac{S_{Hg\infty}}{P_d}\right)^2$
Pittman model	$\lg r_{apex} = -0.117 + 0.475\lg K - 0.099\lg\varphi$
Razaee Model	$\lg K = -1.92 + 0.949\lg\varphi + 0.18\lg R_{10}$
Guo model	$K = C\times(\frac{S_{Hg}}{P_c^2})_{\max}^{D}$
Coates model	$K = \left[(\frac{\varphi}{C})^2\left(\frac{FFI}{BVI}\right)\right]^2$
SDR model	$K = aT_{2gm}^2\varphi^4$

Compared with HPMI technology, NMR technology can quantitatively characterize free fluid and bound fluid in tight reservoirs. Coates et al. [9] found that the permeability of sandstone is controlled by the volume ratio of movable fluid to bound fluid (FFI/BVI) and

proposed the Coates model. The SDR model is a permeability calculation model based on the geometric mean of T_2 (T_{2gm}) [29]. Different scholars have established various improvement models for different regions based on the Coates model or SDR model. These NMR permeability models tend to be less effective in tight sandstones than in conventional sandstones.

These models essentially predict permeability based on a certain characteristic pore throat radius combined with porosity but ignore the heterogeneity of the pore structure. Therefore, the application of these methods in tight reservoirs is limited. The fractal theory proposed by Mandelbrot [30] has been widely used to characterize the heterogeneity of porous media [31,32]. Within a certain range of pore sizes, the pore space of tight sandstone is self-similar; that is, there is 'scale invariance'. Pape et al. [33] first used porosity and fractal dimensions to predict permeability. However, permeability prediction models established by fractal characteristics remain rare.

In this paper, we selected Chang 7 tight sandstones from the Longdong area in the Ordos Basin to analyze the influence of pore structure parameters and fractal dimensions on permeability by integrating casting thin section (CTS), SEM and HPMI experiments. On this basis, a new permeability prediction model was established based on the medium pore throat volume and its fractal dimension. Furthermore, we compared the prediction results of the new model with those of earlier models based on mean absolute percentage error (MAPE), root mean square error (RMSE) and correlation coefficient (R^2) analyses. Finally, we further discuss the advantages of the new model in predicting permeability.

2. Geological Background

The Ordos Basin is located in the western North China block, which is a multicycle superimposed petroliferous basin with stable subsidence and depression migration (Figure 1). The Chang 7 oil layers were formed in the period of the most intense expansion of the lake basin. The lithology is mainly composed of dark mudstone and black shale, with thin layers of fine sandstone and siltstone [34,35]. The Chang 7 oil layers can be subdivided into three subsections: Chang 7_1 subsection, Chang 7_2 subsection and Chang 7_3 subsection. The selected tight sandstone samples are from the Chang $7_{1\text{-}2}$ subsections and are gravity flow deposits of semi-deep lake to deep lake facies. The Chang 7_3 subsection mainly deposits organic-rich black shale and dark mudstone, which is a high-quality source rock section.

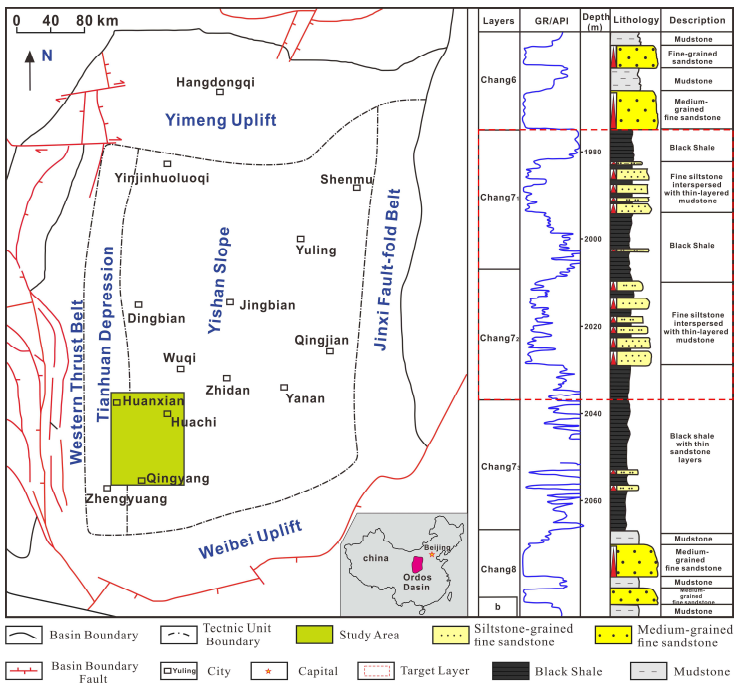

Figure 1. Location of the study area and lithological characteristics of Chang 7 member (modified from Gao et al. [36]).

The lithology of Chang 7 tight sandstone is dominated by lithic arkose and feldspathic litharenite. The debris is mainly quartz, followed by feldspar and rock fragments. The rock debris is mainly composed of dolomite and phyllite. The matrix is mainly composed of hydromica (average 11.7 vol%). A large amount of carbonate cement (up to 30 vol%) can be observed in some samples.

3. Results

3.1. Physical Properties

A total of 34 core samples from Chang 7 member were analyzed for porosity and permeability. The porosity of the selected samples in the study area was between 2.4% and 11.1%, with a mean of 7.7%. The permeability ranged between 0.0021 mD and 0.104 mD, with a mean of 0.0418 mD. Thus, Chang 7 tight sandstone belongs to a low-porosity and ultra-low-permeability reservoir. The relationship between permeability and porosity is poor. The permeability with a similar porosity spans two orders of magnitude (Figure 2), indicating that Chang 7 tight sandstone has strong heterogeneity.

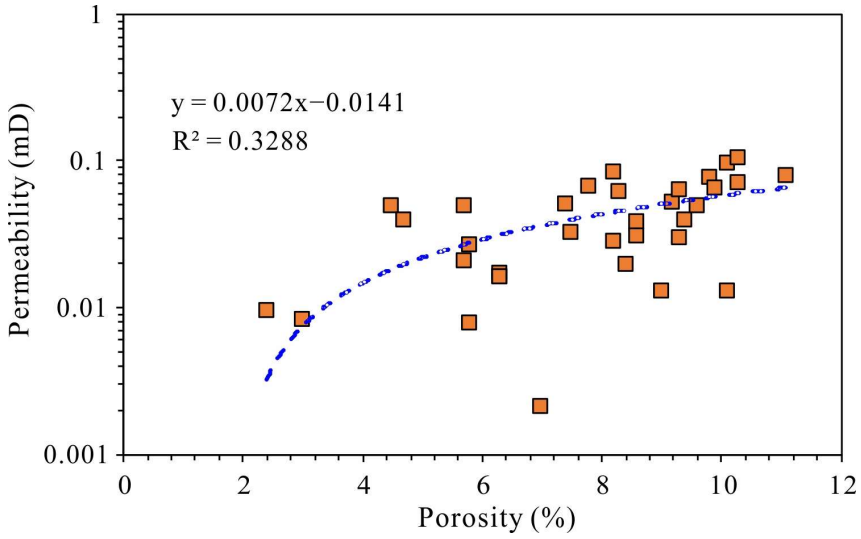

Figure 2. The correlation between permeability and porosity of Chang 7 tight sandstone in the study area. All symbols represent porosity and permeability data for different samples. The blue dashed line reflects the fitted trend line of porosity and permeability data.

3.2. Pore Types

The observations of CTS and SEM of Chang 7 tight sandstones show that the pore types are diverse but not well developed, mainly including dissolution pores (DPs), residual intergranular pores (RIPs), intercrystalline pores (IPs) and a small amount of microfractures. RIPs are usually triangular or polygonal with smooth and straight edges (Figure 3a,c,d). Due to strong compaction and cementation, RIPs only develop in samples with better particle sorting and higher rigid particle content [37]. DPs are the most important pore space in Chang 7 tight sandstones. Dissolution pores in the study area are mainly formed by the partial or complete dissolution of feldspar and rock fragment. DPs have better connectivity and larger pore sizes, mainly distributed between 1 μm and 100 μm (Figure 3a,c,e). IPs are mainly formed between authigenic clay mineral, and their pore diameters are mainly below 300 nm (Figure 3b). There are also a small number of micro-fractures developed in the study area, and the widths are mostly greater than 0.5 μm. (Figure 3c,f).

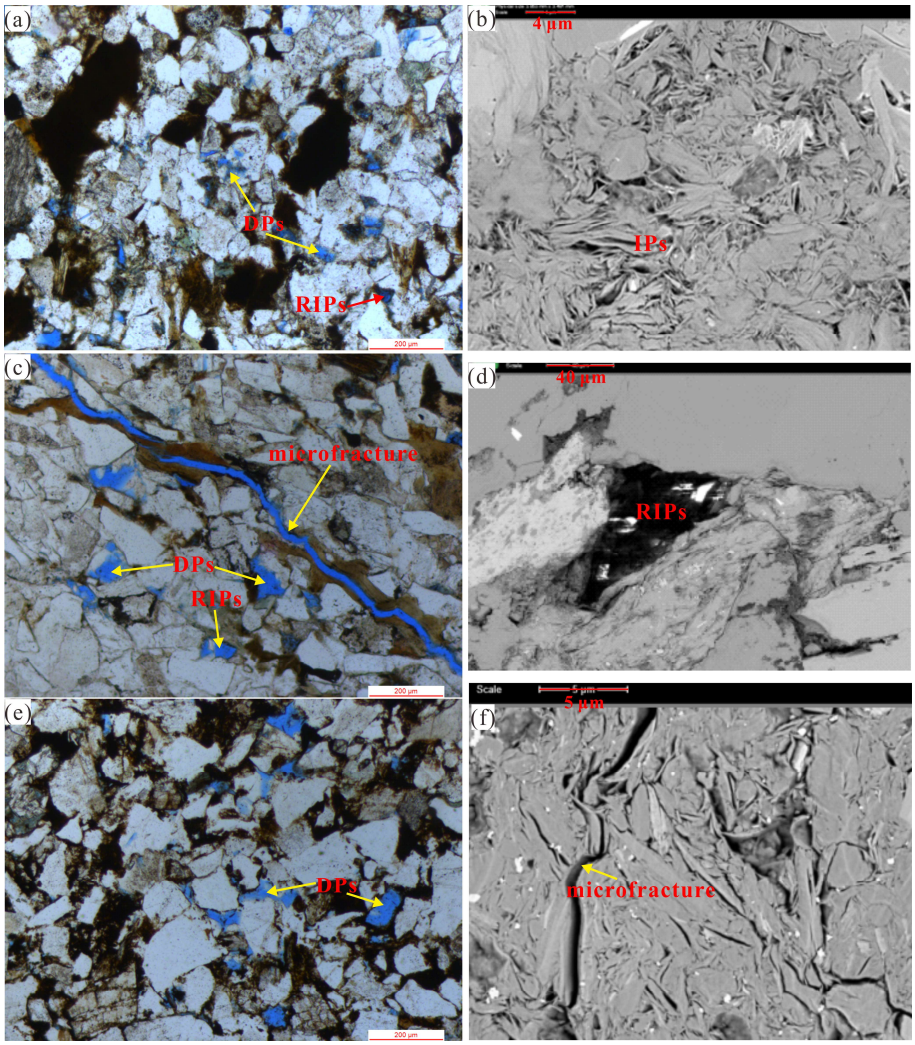

Figure 3. The main diagenesis and pore types of Chang 7 tight sandstone; (**a**) dissolution pores and residual intergranular pores, L1, 2082.42 m, casting thin section; (**b**) intercrystalline pores in clay minerals, L8, 2279.57 m, SEM; (**c**) microfractures, intergranular pores, L13, 1987.87 m, casting thin section; (**d**) residual intergranular pores, L6, 2246.7 m, SEM; (**e**) dissolution pores, L31, 1808.67 m, casting thin section; (**f**) microfractures, L6, 2246.7 m, SEM.

3.3. High-Pressure Mercury Injection Experiment

HPMI experiments were performed on 22 samples using an Auto-pore IV 9500 mercury porosimeter. The interfacial tension was 480 × 10^{-3} N/m and the contact angle of mercury was 140°. The maximum mercury injection pressure was about 200 MPa, and the corresponding pore throat radius was about 3.7 nm. The mercury intrusion curve can be generally divided into three parts: initial rising section, middle plateau section and end upwarping section. According to the shape of the mercury intrusion curve, the distribution and connectivity characteristics of the sample pore throats can be judged. The maximum mercury saturation of Chang 7 tight sandstones was in the range of 33.22%~84.35%, with a mean of 64.71%. The displacement pressure varied from 0.67 MPa to 27.54 MPa, with a mean of 5.54 MPa. As the physical properties of the sample gradually deteriorated, the maximum mercury saturation decreased but the displacement pressure increased (Figure 4). In addition, the mercury withdrawal efficiency was mostly less than 40%, and the average pore throat radius ranged from 0.008 μm to 0.163 μm, showing that Chang 7 tight sandstone has fine pore throats and poor connectivity.

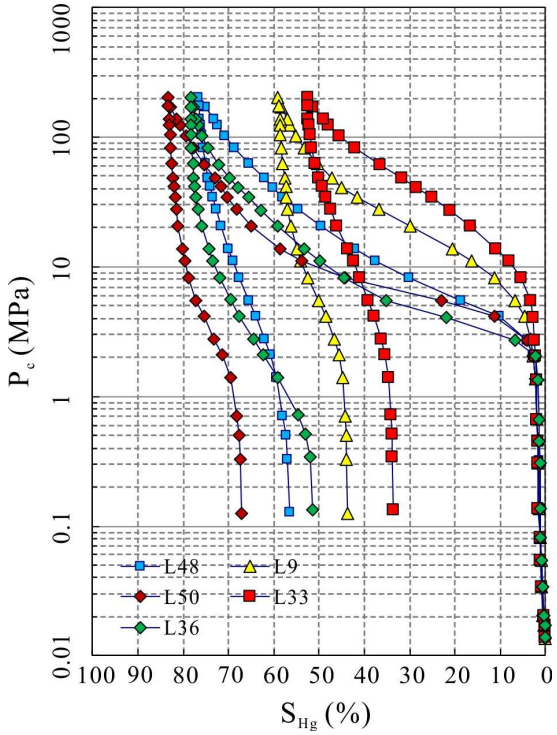

Figure 4. High-pressure mercury intrusion and withdrawal curve of typical samples.

As shown in Figure 5, the permeability shows a good positive correlation with the maximum pore throat radius, average pore throat radius and median pore throat radius, with R^2 of 0.4251, 0.6110 and 0.6021, respectively. In addition, permeability and the sorting coefficient show a weak positive correlation, with an R^2 of 0.1663. These results indicate that the pore throat size plays an important role in controlling permeability.

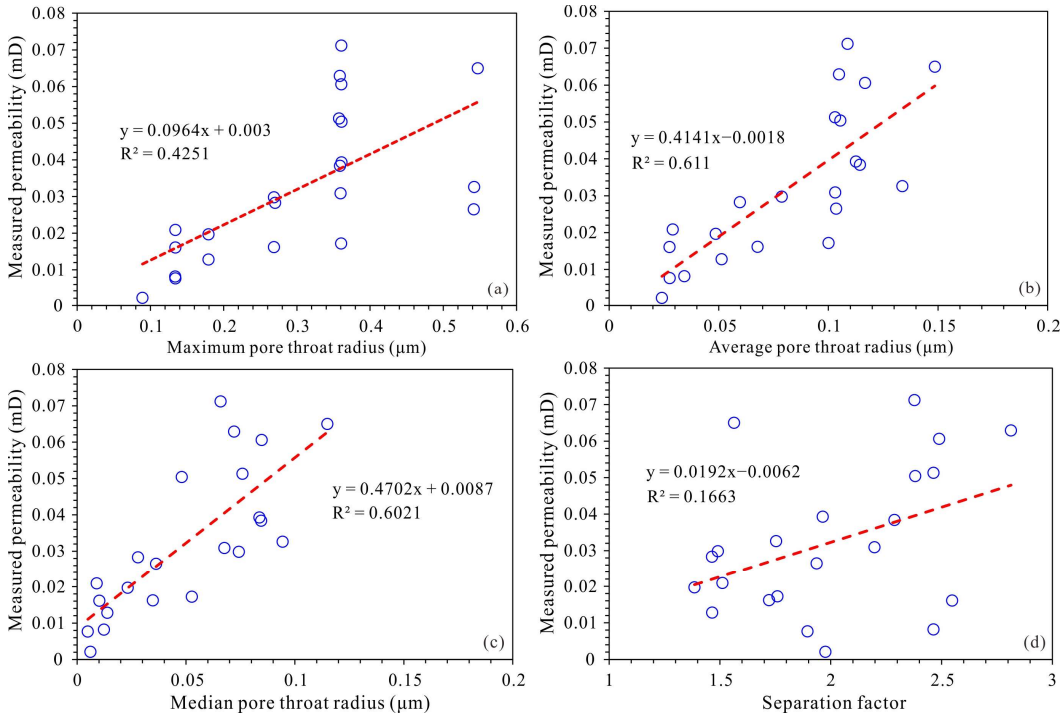

Figure 5. The relationships between permeability and the maximum pore throat radius (**a**) and the average pore throat radius (**b**) and the median pore throat radius (**c**) and the sorting coefficient (**d**).

3.4. Fractal Characteristics and Pore Throat System Classification

Fractal theory can be used to analyze the heterogeneity and self-similarity of a complex pore throat system. Generally, the *D* values of the pore throat system are between two and three. The closer the *D* value is to two, the weaker the heterogeneity of the porous rock is. But the closer the *D* value is to three, the stronger the heterogeneity of the porous rock is [38–40].

D value can be calculated based on HPMI data [41], and the equation is as follows:

$$\lg(100 - S_{Hg}^{r+}) = (3 - D)\lg(r) - (3 - D)\lg r_{\max} \quad (1)$$

where r is the pore throat radius, μm; $S_{Hg}{}^{r+}$ is the mercury saturation of a pore throat with radius > r, %; D is the fractal dimension, dimensionless; and r_{max} is the maximum pore throat radius, μm.

The relationship between $\log(100 - S_{Hg}{}^{r+})$ and $\log(r)$ is displayed in Figure 6. The Chang 7 samples show three-stage fractal characteristics, and there are some differences in the fractal inflection points of different samples. The first inflection point (T1) is in the range of 0.0891~0.1340 μm, while the second inflection point (T2) is in the range of 0.3606~0.5482 μm. According to the two inflection points, the pore throat system of Chang 7 tight sandstone was divided into small pore throats, medium pore throats and large pore throats. The fractal dimensions of small pore throats, medium pore throats and large pore throats were named D1, D2 and D3, respectively. Among them, D1 was distributed between 2.652 and 2.870, with a mean of 2.755; D2 ranged from 2.378 to 2.997, with a mean of 2.797; and D3 ranged from 2.993 to 2.999, with a mean of 2.996. All the samples showed the largest D3 value, indicating that the heterogeneity of the large pore throat was the strongest.

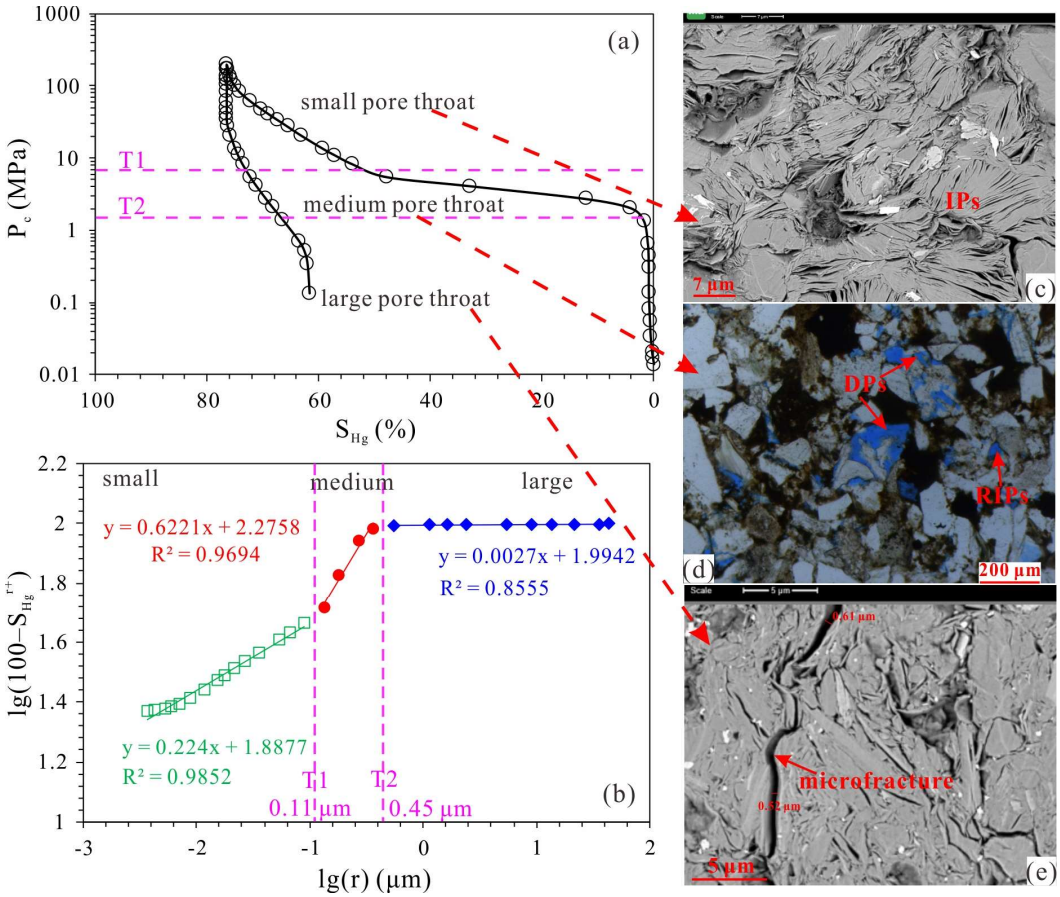

Figure 6. The mercury intrusion curves (**a**), fractal characteristics (**b**), and the corresponding microscopic photos (**c**–**e**) of Sample L6.

The large pore throats correspond to the initial rising section. Due to the lower mercury injection pressure and mercury injection volume, we believe that the large pore throats mainly reflect the fracture system (Figure 6a,b,e). The medium pore throats correspond to the middle plateau section and have characteristics showing that a small change in the mercury injection pressure corresponds to a large amount of mercury injection. Therefore, the medium pore throats are dominated by DPs and RIPs (named the conventional pore throat system), which have large pore throat ratios (Figure 6a,b,d). The small pore throat corresponds to the end upwarping section and has characteristics showing that a large change in mercury injection pressure corresponds to a small amount of mercury injection. The small pore throats are mainly composed of clay IPs and nanoscale intragranular dissolution pores (named the tree-shaped pore throat system) (Figure 6a–c).

We further analyzed the relationships between different pore throat volumes and permeability. The pore throat volumes are given as follows:

$$\mathrm{V1} = \int_{r_{min}}^{\mathrm{T1}} f(r)dr \tag{2}$$

$$\mathrm{V2} = \int_{\mathrm{T1}}^{\mathrm{T2}} f(r)dr \tag{3}$$

$$\mathrm{V3} = \int_{\mathrm{T2}}^{r_{max}} f(r)dr \tag{4}$$

where V1 is the volume of the small pore throat, mL; V2 is the volume of the medium pore throat, mL; V3 is the volume of the large pore throat, mL; $f(r)$ is the volume of a pore throat with radius r; and r_{min} is the minimum pore throat radius, μm.

Permeability displays a weak positive correlation with V3, with an R^2 of 0.2932 (Figure 7b). Permeability has an excellent positive correlation with V2, with an R^2 of 0.7537 (Figure 7a). However, there is no obvious correlation between permeability and V1 (Figure 7a). These results indicate that the permeability of Chang 7 tight sandstone is mainly contributed by the medium pore throat.

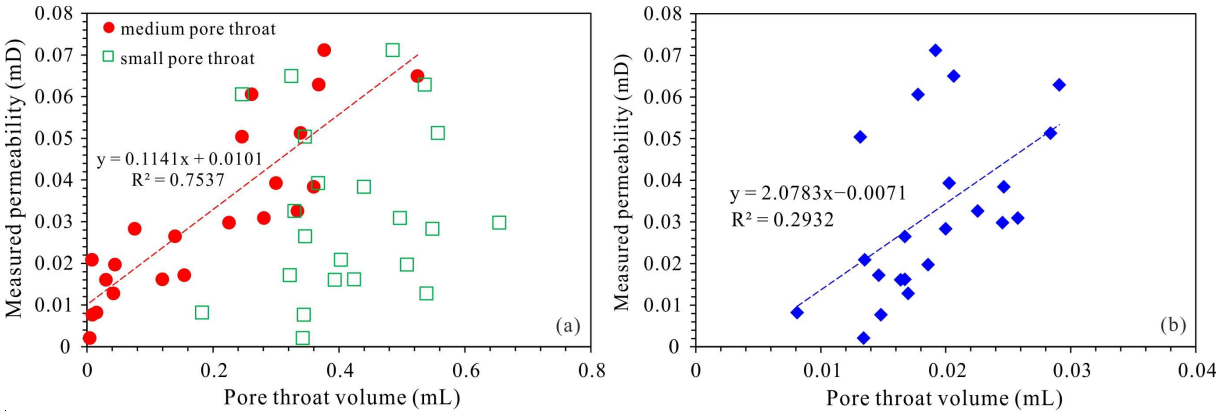

Figure 7. The correlation diagram between the measured permeability and different pore throat volumes. (**a**) Measured permeability versus medium pore throat and small pore throat, and (**b**) measured permeability versus large pore throat.

Permeability has an obvious negative correlation with D2 but has no obvious correlation with D1 and D3 (Figure 8), indicating that the stronger the heterogeneity of the medium pore throat, the lower the permeability of the sample.

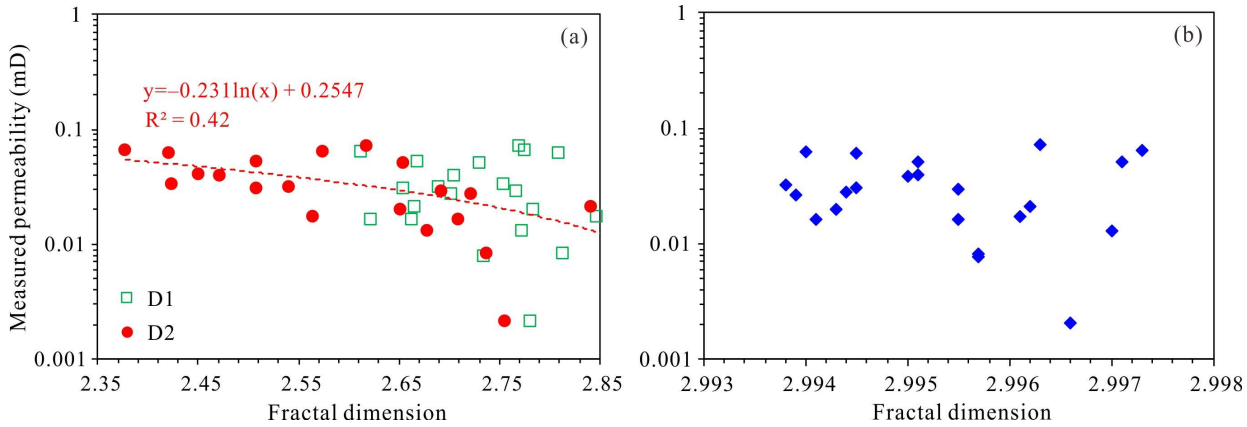

Figure 8. The relationship between measured permeability and fractal dimension. (**a**) D1 and D2, and (**b**) D3. Blue symbols represent measured permeability and D3 data for different samples.

4. Discussion

4.1. Evaluation Criteria for the Prediction Effect of the Permeability Model

Due to the large differences in the pore structure of tight reservoirs in different regions, the applicability of different permeability prediction models varies greatly. Therefore, it is necessary to evaluate the prediction effects of various models to select the most suitable permeability prediction model for the study area. At present, RMSE and MAPE are commonly used as the basis to analyze the applicability of different permeability prediction models.

RMSE mostly represents the square root of the ratio of the square of the deviation between the predicted value and the measured value and the number of observations (n). MAPE refers to the average value of the absolute error between the predicted value and the measured value. Therefore, the smaller the values of RMSE and MAPE, the closer the predicted value is to the measured value.

The calculation equations for RMSE and MAPE are as follows:

$$RMSE = \sqrt{\frac{\sum_{i-1}^{n} (K_{meas} - K_{pred})}{n}} \tag{5}$$

$$MAPE = \frac{1}{n}\sum_{i=1}^{2} \left| \frac{K_{meas} - K_{pred}}{K_{meas}} \times 100 \right| \tag{6}$$

where K_{meas} is the measured permeability of the core samples, mD; K_{pred} is the predicted permeability of the model, mD; and n is the total number of core samples.

4.2. Permeability Prediction Based on Early Models

Figure 9 displays a plot of measured permeability versus predicted permeability using the Pittman model, Winland model and Rezaee model. In the Pittman model, the predicted permeability is significantly lower than the measured permeability. Moreover, the RMSE and MAPE are 0.139 and 117.9%, respectively. For the Winland model, the relationship between the predicted permeability and the measured permeability is discrete, and the error is large (RMSE = 0.545, MAPE = 89%). Obviously, the Winland and Pittman models are not suitable for predicting permeability in the study area. For the Rezaee model, the relationship between the predicted permeability and the measured permeability is better. However, when the permeability is lower than 0.02 mD, the results predicted by the Rezaee model seriously deviate from the measured permeability. Therefore, the Rezaee model is not suitable for predicting samples with low permeability.

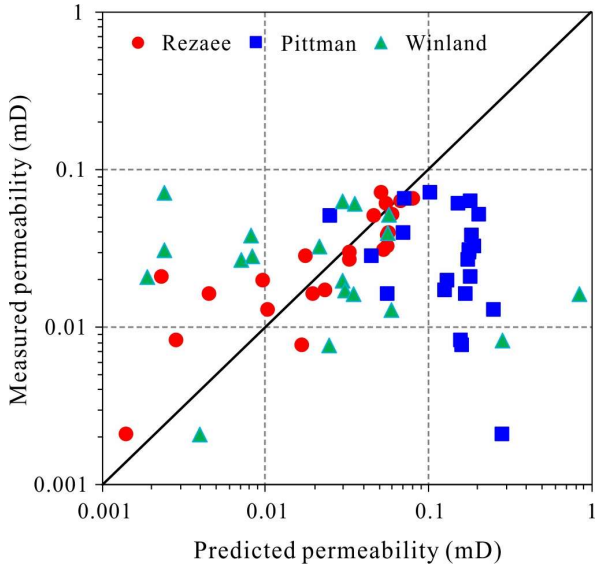

Figure 9. Relationships between measured permeability and predicted permeability derived from the Winland model, Pittman model and Rezaee model.

Based on the above analysis, among the selected early permeability models, the Rezaee model has the best prediction effect. However, for tight sandstones with extremely low permeability (<0.02 mD), the permeability predicted by the three models all have large errors.

4.3. Permeability Prediction Based on R_n Model Derived from HPMI Parameter

Referring to the Winland model and the Rezaee model, mercury saturations of 5% to 50% (in 5% intervals) were chosen to establish a better correlation between measured permeability, porosity and R_n:

$$Log(K) = ALog(R_n) + BLog(\varphi) + C \quad (7)$$

where K is the measured permeability, mD; R_n denotes the pore throat radius at mercury injection saturation of n%, μm; φ is the porosity, %; A, B and C are the parameters obtained by multiple linear regression.

Table 2 presents a series of multiple regression equations and the corresponding R^2 and RMSE and MAPE between the measured and predicted permeability. From the R_5 model to the R_{50} model, R^2 decreased from 0.7485 to 0.6474, RMSE increased from 0.01096 to 0.01230 and MAPE increased from 59.83% to 82.28%, showing that as the pore throat radius decreases, the permeability prediction effect of the R_n model becomes worse. These results further prove that the permeability of tight reservoirs is mainly contributed by some larger pore throats [42]. Therefore, the R_5 model is the model with the highest accuracy among all R_n models in predicting the permeability of the Chang 7 tight reservoir. However, the R_5 model significantly overestimates the permeability of extremely low permeability samples (K < 0.02 mD) (Figure 10).

Table 2. Multiple regression equations and the corresponding R^2 and RMSE and MAPE between measured and predicted permeability.

Model	Equation	R^2	RMSE	MAPE (%)
R_5	$LogK = 0.859 \times LogR_5 + 0.868 \times Log\varphi - 1.670$	0.7483	0.01096	59.83
R_{10}	$LogK = 0.842 \times LogR_{10} + 0.851 \times Log\varphi - 1.629$	0.7462	0.01102	60.31
R_{15}	$LogK = 0.822 \times LogR_{15} + 0.832 \times Log\varphi - 1.587$	0.7431	0.01106	60.64
R_{20}	$LogK = 0.795 \times LogR_{20} + 0.808 \times Log\varphi - 1.542$	0.7383	0.01116	61.52

Table 2. *Cont.*

Model	Equation	R^2	RMSE	MAPE (%)
R_{25}	$LogK = 0.760 \times LogR_{25} + 0.779 \times Log\varphi - 1.497$	0.7312	0.01127	62.49
R_{30}	$LogK = 0.712 \times LogR_{30} + 0.742 \times Log\varphi - 1.453$	0.7204	0.01145	64.04
R_{35}	$LogK = 0.642 \times LogR_{35} + 0.692 \times Log\varphi - 1.416$	0.7034	0.01172	66.64
R_{40}	$LogK = 0.545 \times LogR_{40} + 0.656 \times Log\varphi - 1.418$	0.679	0.01212	70.88
R_{45}	$LogK = 0.383 \times LogR_{45} + 0.753 \times Log\varphi - 1.629$	0.6601	0.01225	76.44
R_{50}	$LogK = 0.265 \times LogR_{50} + 0.895 \times Log\varphi - 1.856$	0.6474	0.01230	82.28

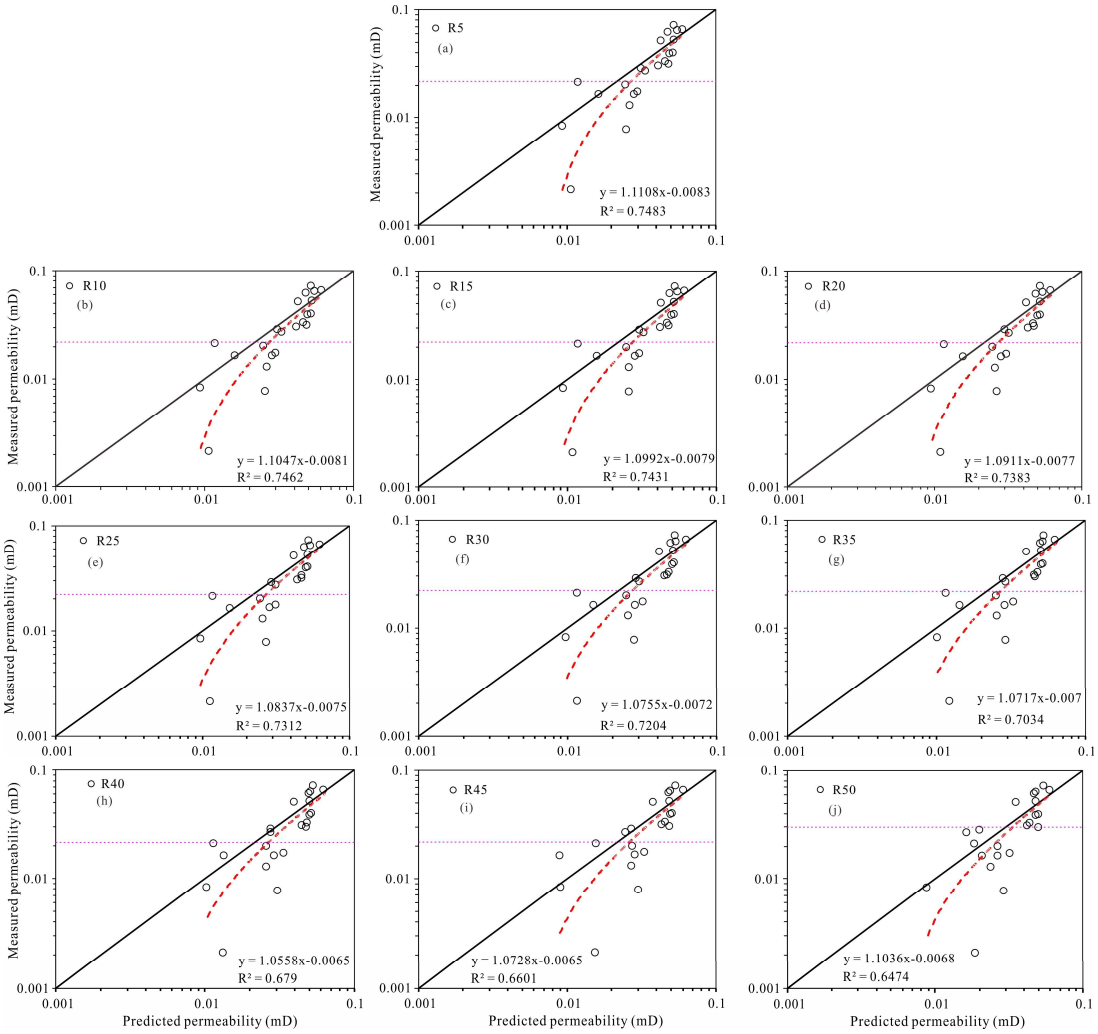

Figure 10. The relationship between measured permeability and predicted permeability derived from the R5~R50 models. (**a**) is from the R5 model, (**b**) is from the R10 model, (**c**) is from the R15 model, (**d**) is from the R20 model, (**e**) is from the R25 model, (**f**) is from the R30 model, (**g**) is from the R35 model, (**h**) is from the R40 model, (**i**) is from the R45 model and (**j**) is from the R50 model.

4.4. Permeability Prediction Model Based on Fractal Dimension

The previous analysis revealed that the measured permeability has the best correlation with D2 and V2; that is, the volume and heterogeneity of the medium pore throat control the permeability of the sample. Therefore, this paper attempts to construct a permeability prediction model using the fractal dimensions and volumes of different pore throats as independent variables (Table 3 and Figure 11).

Table 3. Equations and parameters of the permeability prediction model based on volume and fractal dimensions of different pore throats.

Model	Equation	R^2	RMSE	MAPE (%)
Large pore throat	$K = -53.515/D_3 + 1.886 \times V_3 + 17.864$	0.2183	0.01645	113.46
Medium pore throat	$K = -0.264/D_2 + 0.144 \times V_2 + 0.106$	0.7773	0.00939	46.81
Small pore throat	$K = -0.142/D_1 + 0.014 \times V_1 + 0.079$	0.0008	0.01978	137.10

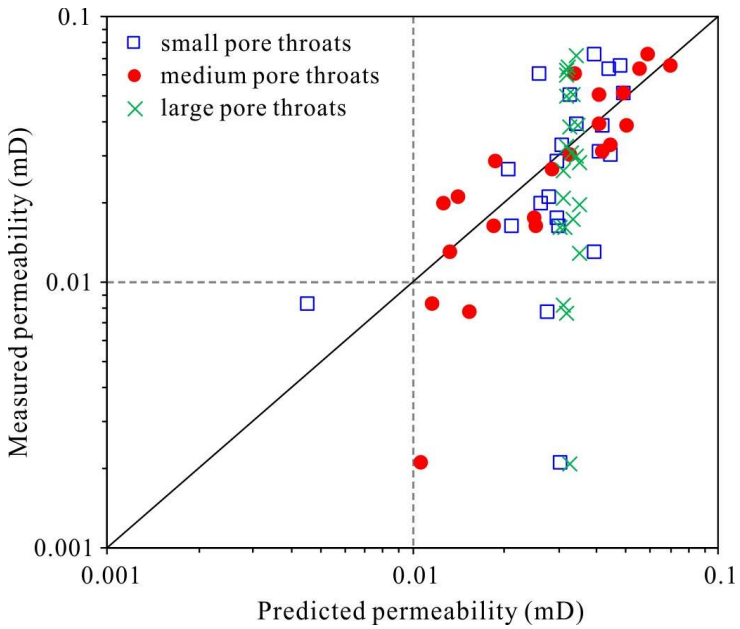

Figure 11. The relationships between measured permeability and predicted permeability based on volume and fractal dimensions of different pore throats.

The equations, R^2, RMSE and MAPE of the three models are displayed in Table 3. The R^2 between the measured permeability and predicted permeability derived from the fractal dimension and volume of medium pore throats is the highest. In addition, the RMSE and MAPE derived from the fractal dimension and volume of medium pore throats are the lowest. In addition, the small pore throat model has the worst permeability prediction effect. Therefore, the permeability of Chang 7 tight sandstone is mainly contributed by medium pore throats, while an increase in small pore throat content will damage the permeability of the reservoir.

4.5. Comparison of Various Permeability Prediction Models

For the Winland model and Pittman model, permeability is strongly affected by pore throat radius (e.g., R_{35} and R_{apex}) and a small coefficient of porosity reduces the contribution of porosity to permeability. The Rezaee and R_n models not only consider the effect of pore throat radius on permeability but also the effect of porosity on permeability. Therefore, the Rezaee and R_n models are better than the Winland model and Pittman model, in predicting permeability. The R_5 model has the best prediction effect on permeability among all R_n models. However, for samples with a different porosity, the pore throat volumes corresponding to a mercury saturation of 5% are different. Simultaneously, the pore structure of Chang 7 tight sandstone is relatively complex, and its pore space is composed of microfractures, RIPs, DPs and IPs. Moreover, different pore spaces contribute differently to permeability. Therefore, it may not be reasonable to directly use porosity as a key parameter to predict permeability. Daigle and Johnson (2016) believed that only when the connected pore throat reaches a certain volume, fluids can flow through the

reservoir [43]. In summary, the R_5 model is not the best among all R_n models for predicting permeability. The new permeability prediction model was constructed using medium pore throat volume and fractal dimension. Medium pore throat volume reflected both the size and volume of the pore throat, and fractal dimension reflected the tortuosity of the medium pore throat. Therefore, the new model predicted permeability with the highest accuracy. Therefore, there are several reasons why models based on medium pore throat volume and fractal dimension are the best at predicting permeability: (1) Fractal dimension can characterize pore structure heterogeneity across scales [44]. Based on multi-stage fractal characteristics, pore throats are classified and the contribution of different pore throats to permeability is clarified. (2) For tight sandstones, the complex pore throat system will make the tortuosity higher. Higher tortuosity reduces fluid mobility. The fractal dimension can reflect the tortuosity of different pore throats to a certain extent [45]. In summary, we believe that a good permeability prediction model should be able to reflect information such as pore throat size, pore throat volume and pore throat shape.

The pore throat system of Chang 7 tight sandstone is composed of several different types of pore throats (large pore throats, medium pore throats and small pore throats). Among them, the medium pore throats contribute the most to permeability, while an increase in the small pore throat content will damage the percolation capacity of the reservoir. Taking sample L36 as an example, its pore throat system is dominated by medium pore throats, accounting for 83.84%, indicating that its percolation network is mainly composed of medium pore throats. Thus, the permeability of sample L36 is high, which is 0.0712 mD. The pore throat system of sample L3 is dominated by small pore throats, accounting for 66.06%, indicating that its percolation network is mainly composed of small pore throats. Therefore, the corresponding permeability is very low, only 0.0161 mD. The proportions of medium pore throats and small pore throats of sample L50 are 48.14% and 46.81%, respectively, indicating that the percolation network is composed of medium pore throats and small pore throats. The permeability of sample L50 is low, which is 0.0298 mD (Figure 12). Therefore, the model constructed using the medium pore throat volume and its fractal dimension as key parameters can accurately predict the permeability of Chang 7 tight sandstone.

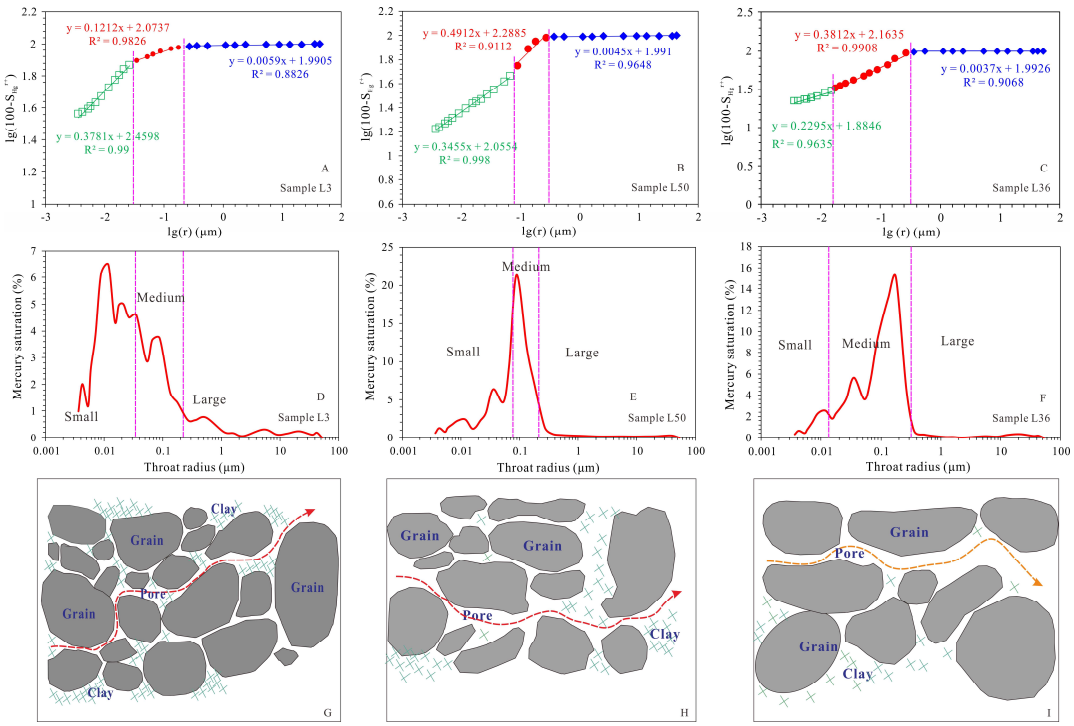

Figure 12. Fractal characteristics (**A**–**C**), pore throat distribution characteristics (**D**–**F**) and fluid percolation diagrams of typical samples (**G**–**I**).

5. Conclusions

1. The pores of Chang 7 tight sandstone are not developed. The pore types are dominated by DPs, followed by IPs, RIPs and microfractures. The pore throat of Chang 7 tight sandstone is characterized by good sorting but small size and poor connectivity.
2. According to the fractal characteristics, the pore throat system is divided into three parts: small pore throats, medium pore throats and large pore throats. Large pore throats are mainly composed of microfractures. Medium pore throats are dominated by DPs and RIPs. Small pore throats are mainly composed of IPs.
3. A good permeability prediction model should be able to reflect information such as pore throat size, pore throat volume and pore throat heterogeneity. The new model based on medium pore throat volume and fractal dimension can accurately predict the permeability of tight sandstones.

Author Contributions: Conceptualization, Z.W.; methodology, W.T.; formal analysis, Y.F.; investigation, Y.Y.; resources, W.T.; data curation, H.G.; writing—original draft, Y.Y.; writing—review & editing, W.T.; supervision, Z.W. and W.T.; project administration, Z.W. and W.T.; funding acquisition, Z.W. and W.T. All authors have read and agreed to the published version of the manuscript.

Funding: This research was funded by the National Natural Science Foundation of China (Grant Nos. 42202187 and 42272160).

Data Availability Statement: Data are contained within the article.

Conflicts of Interest: The authors declare no conflicts of interest.

References

1. Jia, C.; Zou, C.; Li, J.; Li, D.; Zheng, M. Assessment criteria, main types, basic features and resource prospects of the tight oil in China. *Acta Pet. Sin.* **2012**, *33*, 343–350. [CrossRef]
2. Chen, Z.J.; Ren, Z.L. Method for calculating single-well producing geological reserves and single-well technically recoverable reserves in tight sandstone gas reservoirs: A case of carboniferous-permian gas reservoirs in yanchang gas field, ordos basin. *Xinjiang Pet. Geol.* **2022**, *43*, 360–367. [CrossRef]
3. Zou, C.; Zhu, R.; Dong, D.; Wu, S. Scientific and technological progress, development strategy and policy suggestion regarding shale oil and gas. *Acta Pet. Sin.* **2022**, *43*, 1675–1686. [CrossRef]
4. US Energy Information Administration. How Much Shale (Tight) Oil Is Produced in The United States? Available online: https://www.eia.gov/tools/faqs/faq.php?id=847&t=6 (accessed on 4 September 2019).
5. Cao, Y.; Zhu, N.; Zhang, S.; Xi, K.; Xue, X. Diagenesis and reserving space characteristics of tight oil reservoirs of permian lucaogou formation in jimusar sag of junggar basin. *China J. Earth Sci. Environ.* **2019**, *41*, 253–266. [CrossRef]
6. Fu, S.; Jin, Z.; Fu, J.; Li, S.; Yang, W. Transformation of understanding from tight oil to shale oil in the member 7 of yanchang formation in ordos basin and its significance of exploration and development. *Acta Pet. Sin.* **2021**, *42*, 561–569. [CrossRef]
7. Meng, Q.; Zhao, B.; Chen, S.; Lin, T.; Zhou, Y.; Qiao, W. Sedimentary enrichment mode and effect analysis of exploration and development: A case study of Fuyu reservoir tight oil in northern Songliao Basin. *Acta Sedimentol. Sin.* **2021**, *39*, 112–125. [CrossRef]
8. Rezaee, R.; Saeedi, A.; Clennell, B. Tight gas sands permeability estimation from mercury injection capillary pressure and nuclear magnetic resonance data. *J. Pet. Sci. Eng.* **2012**, *88*, 92–99. [CrossRef]
9. Coates, G.R.; Galford, J.; Mardon, D.; Marschall, D. A new characterization of bulk-volume irreducible using magnetic resonance. *Log. Anal.* **1998**, *39*, 51–63.
10. Xie, R.; Zhang, S.F.; Zhou, L.; Liu, H.T.; Yao, M.J.; Jiang, X.G. Hydrocarbon accumulation characteristics of tight reservoirs of da'anzhai member of jurassic ziliujing formation in eastern Sichuan Basin. *Lithol. Reserv.* **2023**, *35*, 108–119. [CrossRef]
11. Zou, C.; Zhu, R.; Liu, K.; Su, L.; Bai, B.; Zhang, X.; Yuan, X.; Wang, J. Tight gas sandstone reservoirs in China: Characteristics and recognition criteria. *J. Pet. Sci. Eng.* **2012**, *88*, 82–91. [CrossRef]
12. Liu, M.; Xie, R.; Wu, S.; Zhu, R.; Mao, Z.; Wang, C. Permeability prediction from mercury injection capillary pressure curves by partial least squares regression method in tight sandstone reservoirs. *J. Pet. Sci. Eng.* **2018**, *169*, 135–145. [CrossRef]
13. Zhang, L.; Lu, S.; Xiao, D.; Gu, M. Characterization of full pore size distribution and its significance to macroscopic physical parameters in tight glutenites. *J. Nat. Gas. Sci. Eng.* **2017**, *38*, 434–449. [CrossRef]
14. Cheng, H.; Wang, F.; Zai, Y.; Zhou, S. Prediction of tight sandstone permeability based on high-pressure mercury intrusion (HPMI) and nuclear magnetic resonance (NMR). *Lithol. Reserv.* **2020**, *32*, 122–132. [CrossRef]
15. He, J.; Ling, K. Measuring permeabilities of Middle-Bakken samples using three different methods. *J. Nat. Gas. Sci. Eng.* **2016**, *31*, 28–38. [CrossRef]
16. Nelson, P.H. Permeability-porosity relationships in sedimentary rocks. *Log. Anal.* **1994**, *35*, 38–62.

17. Hui, G.; Chen, Z.; Wang, Y.; Zhang, D.; Gu, F. An integrated machine learning-based approach to identifying controlling factors of unconventional shale productivity. *Energy* **2023**, *266*, 126512. [CrossRef]
18. Wang, H.; Wang, S.; Chen, S.; Hui, G. Predicting long-term production dynamics in tight/shale gas reservoirs with dual-stage attention-based TEN-Seq2Seq model: A case study in Duvernay formation. *Geoenergy Sci. Eng.* **2023**, *223*, 211495. [CrossRef]
19. Lala, A.M.S.; El-Sayed, N.A. Controls of pore throat radius distribution on permeability. *J. Pet. Sci. Eng.* **2017**, *157*, 941–950. [CrossRef]
20. Wang, W.; Xu, Z.; Li, W.; Hou, T.; Li, Y.; Bai, Y.; Zhu, Y. Determination of permeability in tight sandstone reservoirs using gaussian process regression and high-pressure porosimetry: A case study of the member-7 of yanchang formation in the Jiyuan area of the ordos basin. *Bull. Geol. Sci. Technol.* **2022**, *41*, 30–37. [CrossRef]
21. Wang, J.; Xi, Z.; Lu, D. Pore structure of shale gas reservoirs revealed by constant-speed mercury injection experiments: A case study of wufeng formation shale from northwestern Hunan Province. *Geol. Explor.* **2021**, *57*, 450–456. [CrossRef]
22. Shao, X.; Pang, X.; Li, H.; Zhang, X. Fractal analysis of pore network in tight gas sandstones using NMR method: A case study from the ordos basin, China. *Energy Fuels* **2017**, *31*, 10358–10368. [CrossRef]
23. Yan, Q.; Zhang, Y.; Fu, H.; Jiang, M.; Wang, J.; Sui, S.; Fu, H.; Hao, R.; Guo, M. High pressure mercury injection and scanning electron microscopy applied to characterize micro-and nano-scale pore throats in tight sandstone reservoirs: A case study of the fourth member of shahejie formation in Yi176 block, zhanhua sag, bohai bay basin. *Pet. Geol. Exp.* **2018**, *40*, 280–287. [CrossRef]
24. Purcell, W. Capillary pressures—Their measurement using mercury and the calculation of permeability therefrom. *J. Pet. Technol.* **1949**, *1*, 39–48. [CrossRef]
25. Swanson, B. A simple correlation between permeabilities and mercury capillary pressures. *J. Pet. Technol.* **1981**, *33*, 2498–2504. [CrossRef]
26. Pittman, E.D. Relationship of porosity and permeability to various parameters derived from mercury injection-capillary pressure curves for sandstone. *AAPG Bull.* **1992**, *76*, 191–198. [CrossRef]
27. Guo, B.; Ghalambor, A.; Duan, S. Correlation between sandstone permeability and capillary pressure curves. *J. Pet. Sci. Eng.* **2004**, *43*, 239–246. [CrossRef]
28. Kolodzie, S., Jr. Analysis of pore throat size and use of the Waxman-Smits equation to determine OOIP in Spindle Field, Colorado. In Proceedings of the SPE Annual Technical Conference and Exhibition, Dallas, TX, USA, 21–24 September 1980.
29. Chang, D.; Vinegar, H.J.; Morriss, C.; Straley, C. Effective Porosity, Producible Fluid and Permeability in Carbonates from Nmr Logging. In Proceedings of the SPWLA 35th Annual Logging Symposium, Tulsa, OK, USA, 19 June 1994; p. SPWLA-1994-A.
30. Mandelbrot, B.B. *The Fractal Geometry of Nature*; WH Freeman: New York, NY, USA, 1982; pp. 1–532.
31. Mandelbrot, B.B. On the geometry of homogeneous turbulence, with stress on the fractal dimension of the iso-surfaces of scalars. *J. Fluid Mech.* **1975**, *72*, 401–416. [CrossRef]
32. Zhang, Q.; Jiao, T.; Huang, H.; Qi, Z.; Jiang, T.; Chen, G.; Zhu, Y.; Jia, N. Pore structure and fractal characteristics of ultralow-permeability sandstone reservoirs in the upper triassic yanchang formation, ordos basin. *Interpretation* **2021**, *9*, T747–T765. [CrossRef]
33. Pape, H.; Clauser, C.; Iffland, J. Permeability prediction based on fractal pore-space geometry. *Geophysics* **1999**, *64*, 1447–1460. [CrossRef]
34. Zhang, K.; Liu, R.; Liu, Z.; Li, B.; Han, J.; Zhao, K. Influence of volcanic and hydrothermal activity on organic matter enrichment in the upper triassic yanchang formation, Southern ordos basin, Central China. *Mar. Pet. Geol.* **2020**, *112*, 104059. [CrossRef]
35. Yang, Y.; Li, W.; Ma, L. Tectonic and stratigraphic controls of hydrocarbon systems in the Ordos basin: A multicycle cratonic basin in central China. *AAPG Bull.* **2005**, *89*, 255–269. [CrossRef]
36. Gao, H.; Zhou, X.; Wen, Z.; Guo, W.; Tian, W.; Li, S.; Fan, Y.; Luo, Y. Classification and evaluation of shale oil reservoirs of the Chang $7_{1\text{-}2}$ Sub-Member in the Longdong area. *Energies* **2022**, *15*, 5364. [CrossRef]
37. Lai, J.; Wang, G.; Ran, Y.; Zhou, Z.; Cui, Y. Impact of diagenesis on the reservoir quality of tight oil sandstones: The case of Upper Triassic Yanchang Formation Chang 7 oil layers in Ordos Basin, China. *J. Pet. Sci. Eng.* **2016**, *145*, 54–65. [CrossRef]
38. Ji, F.; Zhang, Y. Application of fractal geometry in description of heterogeneity. *J. Univ. Pet. China Ed. Nat. Sci.* **1994**, *18*, 161–168.
39. Mandelbrot, B.B.; Passoja, D.E.; Paullay, A.J. Fractal character of fracture surfaces of metals. *Nature* **1984**, *308*, 721–722. [CrossRef]
40. Huang, J.; Dong, D.; Li, J.; Hu, J.; Wang, Y. Reservoir fractal characteristics of continental shale: An example from triassic xujiahe formation shale, Sichuan Basin, China. *Nat. Gas. Geosci.* **2016**, *27*, 1611–1618. [CrossRef]
41. Tian, W.; Wen, Z.; Luo, Y.; Xi, Y.; Han, X. The grading evaluation of physical properties of tight sandstone in chang 7 member of wujiao area in ordos basin. *J. Yangtze Univ. (Nat. Sci. Ed.)* **2021**, *18*, 24–32.
42. Xi, K.; Cao, Y.; Haile, B.G.; Zhu, R.; Jahren, J.; Bjørlykke, K.; Zhang, X.; Hellevang, H. How does the pore-throat size control the reservoir quality and oiliness of tight sandstones? The case of the Lower Cretaceous Quantou Formation in the southern Songliao Basin, China. *Mar. Pet. Geol.* **2016**, *76*, 1–15. [CrossRef]
43. Daigle, H.; Johnson, A. Combining mercury intrusion and nuclear magnetic resonance measurements using percolation theory. *Transp. Porous Media* **2015**, *111*, 669–679. [CrossRef]

44. Zhou, N.; Lu, S.; Wang, M.; Liu, W.; Guan, Y.; Tan, H.; Wang, Z. Applicability of fractal capillary pressure models to sandstones. *J. Pet. Sci. Eng.* **2020**, *185*, 106626. [CrossRef]
45. Pape, H.; Riepe, L.; Schopper, J.R. Theory of self-similar network structures in sedimentary and igneous rocks and their investigation with microscopical and physical methods. *J. Microsc.* **1987**, *148*, 121–147. [CrossRef]